Addressing the voltage and energy fading of Al-air batteries to enable seasonal/annual energy storage

Cheng Xu [a,b], Niklas Herrmann [a,c], Xu Liu [a,b,**], Birger Horstmann [a,c,d], Stefano Passerini [a,b,e,*]

[a] Helmholtz Institute Ulm (HIU), Electrochemistry I, 89081, Ulm, Germany
[b] Karlsruhe Institute of Technology (KIT), 76021, Karlsruhe, Germany
[c] German Aerospace Center, 70569, Stuttgart, Germany
[d] Institute of Electrochemistry, Ulm University, Albert-Einstein-Allee 11, 89069, Ulm, Germany
[e] Sapienza University, Chemistry Department, Piazzale A. Moro 5, I-00185, Rome, Italy

Keywords:
Al-air batteries
Seasonal/annual energy storage
Voltage decay
Aluminate
Seeded precipitation process

A B S T R A C T

Al-air batteries are promising candidates for seasonal and annual energy storage. However, severe voltage decay upon discharge limits their practical specific energy. Herein, we first explore the effect of different $Al(OH)_4^-$ concentrations in alkaline electrolytes on the electrochemical oxidation of Al metal anodes (AMAs). Simulation analysis on the electrochemical impedance spectra of AMAs reveals that the formation of $Al(OH)_4^-$ reduces the OH^- concentration and negatively affects the reaction kinetics of AMAs, which is responsible for increased potentials of AMAs and the consequent voltage decay of Al-air batteries. Subsequently, a seeded precipitation process taking advantage of the lower solubility of $Al(OH)_4^-$ at 20 °C than at 50 °C is proposed to recover the voltage decay of Al-air batteries. Inductively coupled plasma atomic emission spectroscopy demonstrates that more than 70 wt % of $Al(OH)_4^-$ in the electrolyte can be removed via this process. Raman spectra and ionic conductivity tests of the electrolyte, together with X-ray diffraction of the precipitate, reveal that the removed $Al(OH)_4^-$ is converted into insoluble $Al(OH)_3$ with release of OH^-. Making use of the precipitation process, Al-air prototypes of Ah-level delivering 3.95 kWh kg_{Al}^{-1} at 50 mA cm^{-2} and 3.52 kWh kg_{Al}^{-1} at 100 mA cm^{-2} are demonstrated.

1. Introduction

Net-zero greenhouse gas emissions target has been adopted by many countries and regional organizations to slow down anthropogenic global warming [1,2]. Its achievement requires a significant increase in renewable energy, e.g., solar and wind energy, and the implementation of sustainable, low-cost, and large-scale storage systems that can balance corresponding fluctuations in electricity generation [3,4]. Various technologies have been proposed to solve this issue, including power-to-X options, i.e., converting renewable electricity into a storable form (e.g., hydrogen), and secondary-battery-based power-to-power options [5–7]. Nonetheless, seasonal and even annual energy storage in a low-cost manner is still a challenge [8]. In this context, employing the earth-abundant, low-cost, and easy to transport and store Al metal as the energy carrier may offer some valuable options, e.g., the combination of Al production via inert-electrode smelting (power to metal) and Al conversion to electricity via Al-air batteries (metal to power) [9–13].

In such a scenario, the specific energy converted from Al via Al-air

* Corresponding author. Helmholtz Institute Ulm (HIU), Electrochemistry I, 89081, Ulm, Germany.
** Corresponding author. Helmholtz Institute Ulm (HIU), Electrochemistry I, 89081, Ulm, Germany.
E-mail addresses: xu.liu@kit.edu (X. Liu), stefano.passerini@kit.edu (S. Passerini).

batteries is a crucial parameter to achieve high round-trip energy efficiency (RTE), which is determined by the cell voltage and the Al utilization efficiency, i.e., the Coulombic conversion efficiency (CE). Alkaline solutions are the most commonly used electrolytes for Al-air batteries, owing to their higher ionic conductivity, better oxygen diffusion, and faster reaction kinetics compared with acidic and neutral electrolytes [14–17]. The electrochemical reaction of Al-air batteries employing alkaline electrolytes can be described as it follows [18,19].

$$4Al + 3O_2 + 4OH^- + 6H_2O \rightarrow 4Al(OH)_4^- \quad (1)$$

This electrochemical reaction is accompanied by a spontaneous chemical reaction between the Al metal anode (AMA) and the electrolyte, i.e., Al self-corrosion, as described below [20].

$$4Al + 12H_2O + 4OH^- \rightarrow 4Al(OH)_4^- + 6H_2\uparrow \quad (2)$$

Both these two reactions lead to the formation of the soluble aluminate, e.g., $Al(OH)_4^-$. When its solubility in the electrolyte is reached, reaction (3) occurs, leading to the formation of insoluble Al $(OH)_3$ [18]:

$$Al(OH)_4^- \rightarrow OH^- + Al(OH)_3\downarrow \quad (3)$$

Due to the spontaneous chemical corrosion (2), AMAs usually suffer from a low CE [21]. However, several strategies have been successfully developed to suppress self-corrosion, such as electrolyte additives and rationally designed Al alloy [22–35]. For instance, ZnO, Sn^{4+}, and organic compounds used as additives for alkaline electrolytes can greatly mitigate AMAs' corrosion [32,33]. Al–Ga, Al–Sn, Al–Zn, and Al–In alloys can significantly improve the CE upon electrochemical oxidation [11]. In addition, the cathode electrocatalysts have also been carefully designed to reduce the overpotential of oxygen reduction reactions [36–40] e.g., noble metals, transition metal oxides, carbon materials and metal-nitrogen doped nano materials [11]. Due to these tremendous efforts, the energy density of Al-air batteries has gained remarkable improvements. However, voltage decay of the Al-air cells during discharge is still commonly reported in the literature [40–42] which severely decreases the practical energy density of Al-air batteries, especially, upon long-term operation [42–45]. Currently, the voltage decay is widely attributed to the accumulation of $Al(OH)_3$ on the surface of AMAs, which blocks further electrochemical reactions [24,46–48]. Nonetheless, such hypothesis and the role of the aluminate still need to be clarified, requiring further experimental evidence.

In this work, the electrochemical behavior of AMAs in KOH aqueous solutions containing various concentrations of dissolved aluminum, predominantly present as $Al(OH)_4$, is firstly compared to investigate the impact of $Al(OH)_4$. It is observed that an increasing polarization of AMAs occurs even before any precipitate is generated on their surface. Further experimental and computational results reveal that the accumulation of $Al(OH)_4$ greatly reduces the OH^- concentration and, in turn, negatively affects the reaction kinetics. Therefore, the voltage decay issue of Al-air batteries is caused by the accumulation of $Al(OH)_4$ in the electrolyte rather than $Al(OH)_3$ on AMAs. Subsequently, it is demonstrated that seeded precipitation of $Al(OH)_4$ in the electrolytes to $Al(OH)_3$ precipitate with releasing OH^- via utilizing its lower solubility at 20 °C than at 50 °C allows effective recovery of the potential of AMAs and the voltage of Al-air batteries. At last, prototype Al-air cells are assembled and tested to evaluate the feasibility of voltage recovery via the proposed seeded precipitation process.

2. Experimental section

2.1. Electrolyte preparation

4 M KOH solution was prepared by adding KOH particles (≥85%, Honeywell) into deionized water. 5 g $Na_2SnO_3{\cdot}3H_2O$ (95%, Aldirich) were dissolved in each liter of the 4 M KOH solution, and the obtained clear solution was named Blank electrolyte. Electrolytes with different $Al(OH)_4^-$ contents was prepared via dissolving high purity Al powder (99.999%, Alfa Aesar) in the blank electrolyte. At 20 °C, the maximum amount of Al power that dissolves in 60 mL of 4 M KOH solutions without precipitate formation) is around 2 g, i.e., 33.4 g L^{-1}. The solutions with 16.7 and 33.4 g L^{-1} of dissolved Al were named as semi-saturated (Semi-S-20) and nearly saturated (S-20) electrolytes, respectively. To suppress the self-corrosion of Al, 5 g L^{-1} $Na_2SnO_3{\cdot}3H_2O$ were added to the above electrolytes before electrochemical tests [49].

The electrolytes for measurements at 50 °C were prepared at 50 °C, which was controlled with an oil bath. The pure Al powder was dissolved in the 4 M KOH solution, and the amount of the added Al powder was 66.7 g for each liter of the 4 M KOH solution. The obtained clear solution was named pre-S-50. With the further addition of 5 g $Na_2SnO_3{\cdot}3H_2O$ per liter of the solution, S-50 was obtained.

The pre-S-50 was also used to check the precipitation process. After standing at 20 °C in an oven for 24 or 48 h, the clear upper solution was extracted and added with 5 g $Na_2SnO_3{\cdot}3H_2O$ per liter of the solution, which was named S-50-s24 and S-50-s48, respectively.

2.2. Electrochemical measurements

Three electrode beaker cells were employed to investigate the electrochemical behavior of AMAs. Al plates (99.997%, 15 × 10 × 1 mm, Thermo scientific), four layers of Ni foam (80 × 40 mm, EDAQ), and leakless Ag/AgCl electrodes (EDAQ) were used as the working, counter, and reference electrodes, respectively. The beaker cells were tested in an oil bath at 50 °C or in an oven at 20 °C with BioLogic SP-200. Electrochemical impedance spectroscopy (EIS) was conducted using a VMP multichannel potentiostat (Bio-Logic). Potentio EIS of AMAs at the open circuit state with static electrolytes was measured with a frequency range of 0.1–10^5 Hz and a voltage amplitude of 5 mV. Galvano EIS of AMAs at a current density of 100 mA cm^{-2} with stirred electrolytes was measured with a frequency range of 0.1–10^5 Hz and a current amplitude of 10 mA (2.94 mA cm^{-2}).

The performance of Al-air full cells was evaluated via a PTFE cell with flow electrolyte. The picture of the cell can be found in the Supporting Information. Al foil exposing 1 cm^2 to the electrolyte and MnO_x@C cathodes exposing 4.5 cm^2 to electrolyte/air were used as the anode and cathode, respectively. The flow rate of the electrolyte was controlled to be 5 cm^3 min^{-1} by a peristaltic pump (Watson Marlow 323). For the short-term (2 h) tests, 40 mL electrolytes were employed. For the long-term tests of the prototype, 10 mL electrolytes were used. The full cells were tested with BioLogic BCS-815. The temperature of the cell and electrolyte tank was controlled via a Binder oven.

For Al-air full batteries long-term discharging at 50 °C, 10 mL Blank was used as the electrolyte at the beginning of discharge. The Al foil was nearly consumed after 8 h at 100 mA cm^{-2} and was therefore replaced with new Al foil as AMAs, in which the electrolyte and cathode were kept unchanged. After discharging for 24 h (equaling to 2.4 Ah), the electrolyte was extracted from the cell for regeneration. Specifically, 1% $Al(OH)_3$ (Merck KGaA) seed was added to the electrolyte, which was placed in an oven at 20 °C for 24 h. Afterward, the mixture was filtered and the clear solution was refilled to the Al-air cell as the regenerated electrolyte. Such electrolyte regeneration was conducted again after discharging for another 8 h.

Two indicators, conversion efficiency (CE) and specific energy (SE), were used to measure the utilization of the Al anode. The CE of Al was calculated by the following equation:

$$CE = \frac{t \times i}{C \times (m_0 \quad m_1)}$$

Where t means the time of Al discharging (h); i is the current (mA); C is the theoretical specific capacity of Al, i.e., 2980 mAh g^{-1}; m_0 and m_1 (g) represent the mass of Al before and after the electrochemical reaction,

respectively.

Specific energy (SE) of the Al-air full cells based on the mass of the consumed Al was calculated by the following equation:

$$SE = \frac{t \times i}{(m_0 \quad m_1)} \times E,$$

where E is the average discharge voltage of the Al-air full battery.

2.3. Characterization

The electrochemical oxidized AMAs were washed with deionized water and ethanol. The morphology of Al powder and anode was observed with scanning electronic microscopy (SEM) Zeiss LEO 1550 microscope equipped with an Energy dispersion X-ray detector. Al content in KOH solutions was measured by ICP-OES. The Raman spectrum was recorded on RAM II FT-Raman module of a Bruker Vertex70v FT-IR spectrometer with a laser wavelength of 1064 nm and laser power of 300 mW. X-ray diffraction (XRD) patterns of the electrode were conducted using a Bruker D8 Advance diffractometer (Bruker, Germany) with Cu-Kα radiation. The change of ions transport of the electrolyte with time at 20 °C was recorded by AMEL 160 conductivity meter, where 0.5 mL electrolyte was sealed inside a glass conductivity cell equipped with two platinized-platinum electrodes.

3. Results and discussion

To mimic the accumulation of aluminates in alkaline electrolytes upon discharge of Al-air batteries, various amounts of high purity Al powder (99.99%, 3–50 μm, Fig. S1) were dissolved in 4 M KOH aqueous solutions, resulting in electrolytes with different $Al(OH)_4$ contents. Al_2O_3 and $Al(OH)_3$ were also explored as the raw materials, but their reaction in 4 M KOH at room temperature was rather slow. At 20 °C, the maximum amount of Al power that dissolves in 60 mL of 4 M KOH solutions without precipitate formation is around 2 g, i.e., 33.4 g L^{-1}. Three different solutions were then prepared with 0, 16.7, and 33.4 g L^{-1} of dissolved Al, which are named as Blank, semi-saturated (Semi-S-20), and nearly saturated (S-20) electrolytes, respectively. To suppress the self-corrosion of Al, 5 g L^{-1} $Na_2SnO_3{\cdot}3H_2O$ were added to the above electrolytes before electrochemical tests [49]. More details about the electrolyte preparation can be found in experimental section.

The electrochemical behavior of AMAs in the above-mentioned electrolytes was first evaluated via three-electrode beaker cells employing an Ag/AgCl electrode as the reference electrode, stacked Ni foam as the counter electrode, and a high-purity Al plate (99.99%) as the working electrode. The potential evolution of the AMAs upon electrochemical oxidation at a current density of 100 mA cm^{-2} for 2 h and 20 °C, are shown in Fig. 1a for the three electrolytes. The average potential and the CE of AMAs are shown in Fig. 1b and S2, respectively. CEs higher than 97% were reached in all the electrolytes, thanks to the effectively suppressed Al corrosion reaction with the addition of $Na_2SnO_3{\cdot}3H_2O$ additive to the electrolytes [50]. The potential of AMAs, however, highly depends on the $Al(OH)_4$ concentration in the electrolyte. Higher concentrations lead to more pronounced over-potentials and faster potential increase along the electrochemical oxidation. The average potential of AMAs upon the tests with the Blank, Semi-S-20, and S-20 electrolytes is 0.97, 0.8, and 0.39 V vs. Ag/AgCl, respectively, demonstrating the negative effect of the aluminate present in the electrolyte. Such effect on AMAs is tightly associated with the voltage decay of Al-air full cells, as demonstrated via Al-air cells employing Al plate anodes, commercial MnO_x-based air cathodes, and the aforementioned electrolytes under flowing conditions (see more details about the full cells in the Experimental Section and Fig. S3 in Supporting Information). MnO_x was selected as the cathode material due to its low cost. The discharge profiles of the Al-Air cells employing the Blank and S-20 electrolytes at 100 mA cm^{-2} are shown in Fig. 1c. The Al-Air cell employing the Blank electrolyte exhibits a steady discharge profile, matching the performance achieved with the beaker cell (Fig. 1a). The average discharge voltage and specific energy based on the mass of consumed Al are calculated to be 0.56 V and 1.65 kWh kg^{-1}, respectively (Fig. S4). In contrast, when the S-20 electrolyte is employed, the voltage of the cell drops to 0 V in 25 s.

The negative effects were previously attributed to the accumulation of $Al(OH)_3$ on the surface of AMAs, which blocks further electrochemical

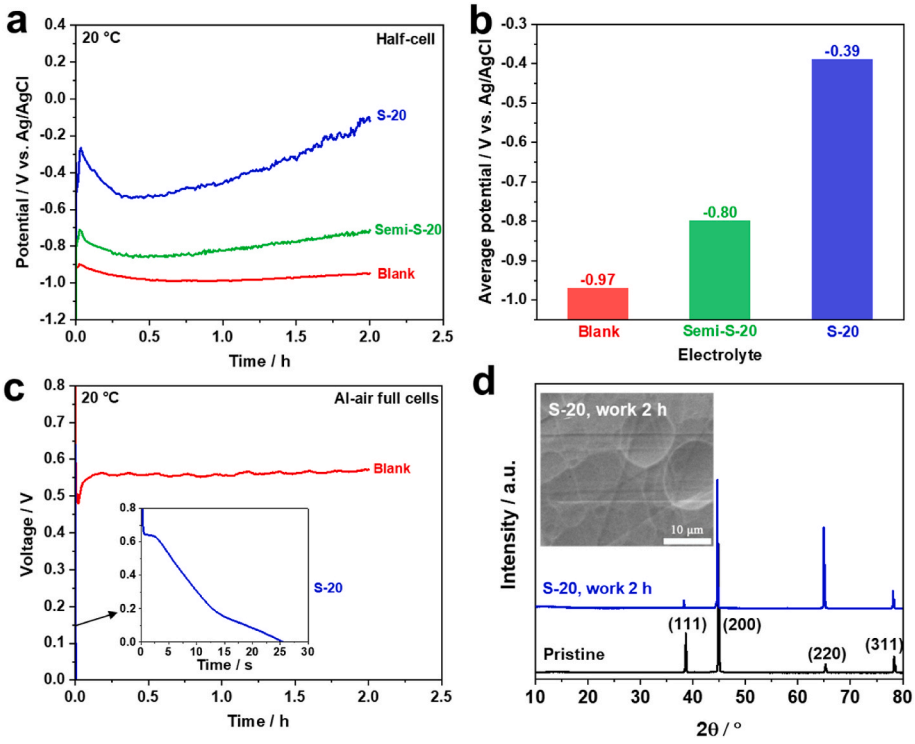

Fig. 1. (a) Potential of AMAs upon electrochemical oxidation at 100 mA cm^{-2} and 20 °C in the beaker cells employing Ni foam as the counter and Ag/AgCl electrode as the reference electrode with the Blank, Semi-S-20, and S-20 electrolytes, and (b) the corresponding average potential. (c) Galvanostatic discharge curves (at 100 mA cm^{-2}) of Al-air cells employing Blank or S-20 electrolytes. (d) XRD of AMAs before and after electrochemical oxidation at 100 mA cm^{-2} and 20 °C for 2 h in the S-20 electrolyte. The inset is a surface SEM image of the AMA after electrochemical oxidation.

reaction. Nonetheless, no precipitate could be observed with the naked eye on the surface of AMA after electrochemical oxidation at 100 mA cm ^{2} for 2 h in the S-20 electrolyte (Fig. S5). In a further step, this sample and the pristine electrode were characterized. Comparing the surface SEM images of the pristine (Fig. S6) and electrochemically oxidized AMAs (inset of Fig. 1d), one can find that the electrochemical oxidation leads to the formation of some oval pits but no additional deposit on the surface of AMAs. The energy dispersion X-ray (EDX) spectrum of the electrochemically oxidized AMA (Fig. S7) shows a composition of 96.8 wt% Al, 2.8 wt% C, and 0.4 wt% O, which excludes the presence of a significant amount of $Al(OH)_3$. As shown in Fig. 1d, only the peaks belonging to metallic Al can be observed in the X-ray diffraction (XRD) patterns. These results reveal that no obvious deposit occurs on the AMA surface even after electrochemical oxidation (for 2 h) in the S-20 electrolyte containing nearly saturated $Al(OH)_4$, implying that the increased polarization of AMAs upon electrochemical oxidation is simply not caused by the accumulation of $Al(OH)_3$ on their surface.

To understand the reasons for the increasing polarization upon accumulation of aluminates in electrolytes, electrochemical impedance spectroscopy (EIS) measurements of AMAs in the beaker cells containing static Blank, Semi-S-20, or S-20 electrolytes at open circuit potential (OCP) were firstly measured (Fig. 2a). All the measured spectra show two distinct semi-circles and an inductive loop at intermediate frequencies similar to the previous literature [51,52]. The high-frequency intercept with the X-axis corresponds to a pure resistor (R_{ohmic}) associated with the bulk resistance of the electrolyte and electrodes. R_{ohmic} increases with $Al(OH)_4$ concentration in the reverse fashion of the ionic conductivity of the electrolytes, i.e., 371, 318, and 264 mS cm ^{1} for Blank, Semi-S-20, and S-20, respectively. This latter decrease is attributed to the formation of $Al(OH)_4$, which is accompanied by the consumption of equal mole of OH (fast ion conductor) in the electrolyte according to equations (1) and (2), while OH exhibits higher molar conductivity with respect to $Al(OH)_4$.

To understand the physico-chemical process of the two semi-circles, additional EIS measurements were carried out with an applied offset current of 100 mA cm ^{2} in stirred electrolytes to avoid concentration gradient effects (Fig. 2b). The high-frequency (HF) semi-circle shrinks under load, which indicates a reaction-rate limited process, e.g., described by Butler-Volmer kinetics. The low-frequency (LF) semi-circle remains constant under load, which indicates a transport-limited process, e.g., described by a finite-length Warburg element Z_W with transmissive boundaries [53]. Such a transport-limited process is not occurring in the bulk electrolyte but in a rather thin region close to the electrode (see later for more details). With these considerations, an overall equivalent circuit, shown in Fig. 2a, is proposed. R_{ohmic} mainly represents the solution resistance. In the second part, C_{dl} is the double layer capacitance of the charge-transfer connection; L is the inductance of the adsorption process; while R_1 and R_2 give the charge transfer resistance ($R_{CT} = \frac{R_1 \cdot R_2}{R_1+R_2}$). Inductive loops in EIS spectra are commonly observed in systems undergoing corrosion where chemical species, ions or molecules, are physically adsorbed at the interface of the electrochemical double layer with a given electrical charge transfer [54]. The inductive loop here represents the adsorption of the intermediates, e.g., $Al(OH)_{x,ads}$ ($x \leq 3$) [55]. The last contribution represents the transport-limited process of the LF semi-circle. We use a Warburg short element Z_W with a diffusion resistance (R_D) instead of the conventional RC equivalent circuit, as the corresponding length scales in the RC case are not physically valid. The measured EIS spectra have been fitted accordingly to the proposed equivalent circuit, and the results are summarized in Tables S3 and S4. Therefore, the potential of AMAs under load consists of the Nernst potential of the aluminum redox reaction, the overpotential from solution resistance η_{elyt}, charge transfer overpotential η_{CT}, and the overpotential from the diffusion layer η_D.

In a further step, their values as a function of $Al(OH)_4$ concentration are simulated according to the results of EIS measurements. The underlying speciation model was adapted from previous works on modelling aqueous zinc batteries [56,57]. with details of the simulation methods provided in Supporting Information. The Nernst potential and electrolyte conductivity are calculated to evaluate the model predictions based on the solved speciation using literature data on stability constants (Table S1, Fig. S8). The approach for the conductivity calculation is validated against measurements of a pure KOH electrolyte. A heuristic model for the pure KOH electrolyte exists in order to compare the simulation results. As the dilute solution model shows accurate

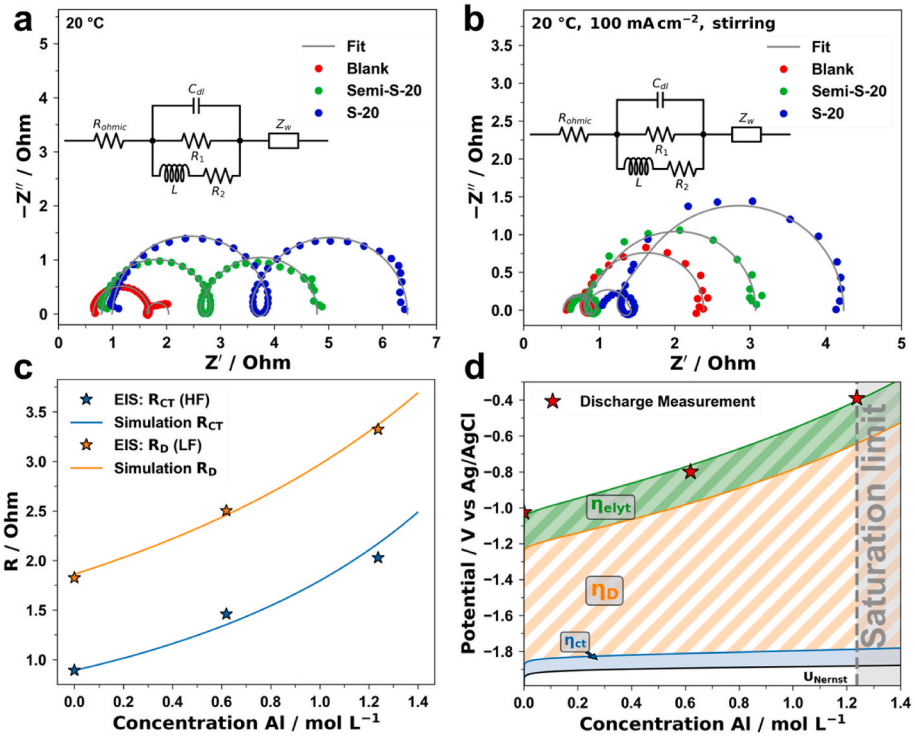

Fig. 2. Nyquist Plot of the EIS of AMAs (a) in static Blank, Semi-S-20, and S-20 electrolytes at OCP and (b) under stirring upon galvanostatic oxidation at 100 mA cm^{-2}. The used equivalent circuit model is shown as an inset. (c) Simulation results for the R_{CT} and R_D value as a function with Al concentration. (d) Simulation results for the discharge potential as a function of Al-content in the electrolyte, shown are the contributions by overpotentials for the charge transport, diffusion, and electrolyte resistance.

predictions (see Fig. S9) for KOH, we can apply this approach to the Al–KOH case. The simulation results clearly show the trend observed both in the conductivity measurements and the EIS data, i.e., the conductivity decreases with increasing electrolytic aluminum content. The individual results for electrolyte conductivity can be found in the supplementary (Fig. S10).

To evaluate the charge transfer characteristics, the exchange current density from the EIS at OCP are calculated to be 8.33 (Blank), 5.09 (Semi-S-20), and 3.66 mA cm ^{2} (S-20), accordingly to equation S7. With these values, R_{CT} can be calculated with our theory based on equation S9. As shown in Fig. 2c, the predicted scaling of charge transfer resistance with Al concentrations is in very good agreement with the experimental results of EIS data, i.e., the R_{CT} derived from the HF semicircle. With equation S11, the diffusion length and diffusivity in the finite-length Warburg regime can be calculated based on the EIS obtained under load. The length (L) is consistently found in the range of 24–43 nm, confirming that the Warburg regime does not extend in the bulk electrolyte, and the effective diffusion coefficient (D) is in the range of 5–9 $\times$ 10 ^{11} cm^{2} s ^{1}. The dependence of the Warburg resistance, i.e., diffusion resistance R_D, on Al concentration is further predicted and compared with the experimental EIS data (Fig. 2c). The model has been parameterized with 1.8 Ω of the Blank electrolyte. In general, the predicted trend of R_{CT} and R_D matches well with the experimental results, which validates the simulation model.

With the simulation of Nernst potential, solution resistance, charge transport resistance, and diffusion resistance (more details can be found in Supporting Information), the expected potential of AMAs subjected to 100 mA cm ^{2} oxidation currents as a function of Al concentration in the electrolytes are further calculated as shown in Fig. 2d. The predicted result is, once more, in good agreement with the experimental potential (red stars). One can see that the increased potential along with Al concentration is mainly caused by the diffusion resistance in the Warburg regime, which is dependent on the concentration of OH (c_{OH}), i.e., $R_D \propto 1/c_{OH}$.

Based on these results, it can be concluded that the presence of $Al(OH)_4$ in the electrolyte reduces the availability of OH , which significantly slows down the kinetics of the electrochemical reaction. Consequently, the AMAs show increasing overpotential leading to voltage decay of the Al-air full cells. As described by equation (3), when $Al(OH)_4$ reaches its saturated concentration in the electrolyte, it will convert to $Al(OH)_3$ precipitates with the release of OH . Such a process could be utilized to recover the decayed voltage of Al-air batteries. In a further step, we propose the conversion of $Al(OH)_4$ to $Al(OH)_3$ and OH according to its solubility difference at different temperatures, as we found that the maximum amount of Al power that could be dissolved by 60 mL 4 M KOH aqueous solution without formation of precipitate was increased from 2 g to 4 g when the solution temperature was increased from 20 to 50 °C.

To check the feasibility of the precipitation process, the electrolyte saturated with aluminum at 50 °C was placed in a climatic chamber at 20 °C. Photographs of the solution after standing at various times were taken and shown in Fig. S11. The initially clear solution without any precipitate became turbid after standing 8 h. After 24 h, the solution became clear again but with a large amount of white precipitate at the bottom of the beaker. The content of Al in the clear upper solution was tested by inductively coupled plasma atomic emission spectroscopy (ICP-OES), and the results are shown in Fig. 3a. In general, Al content in the solution decreased with standing time (Fig. 3a). After standing at

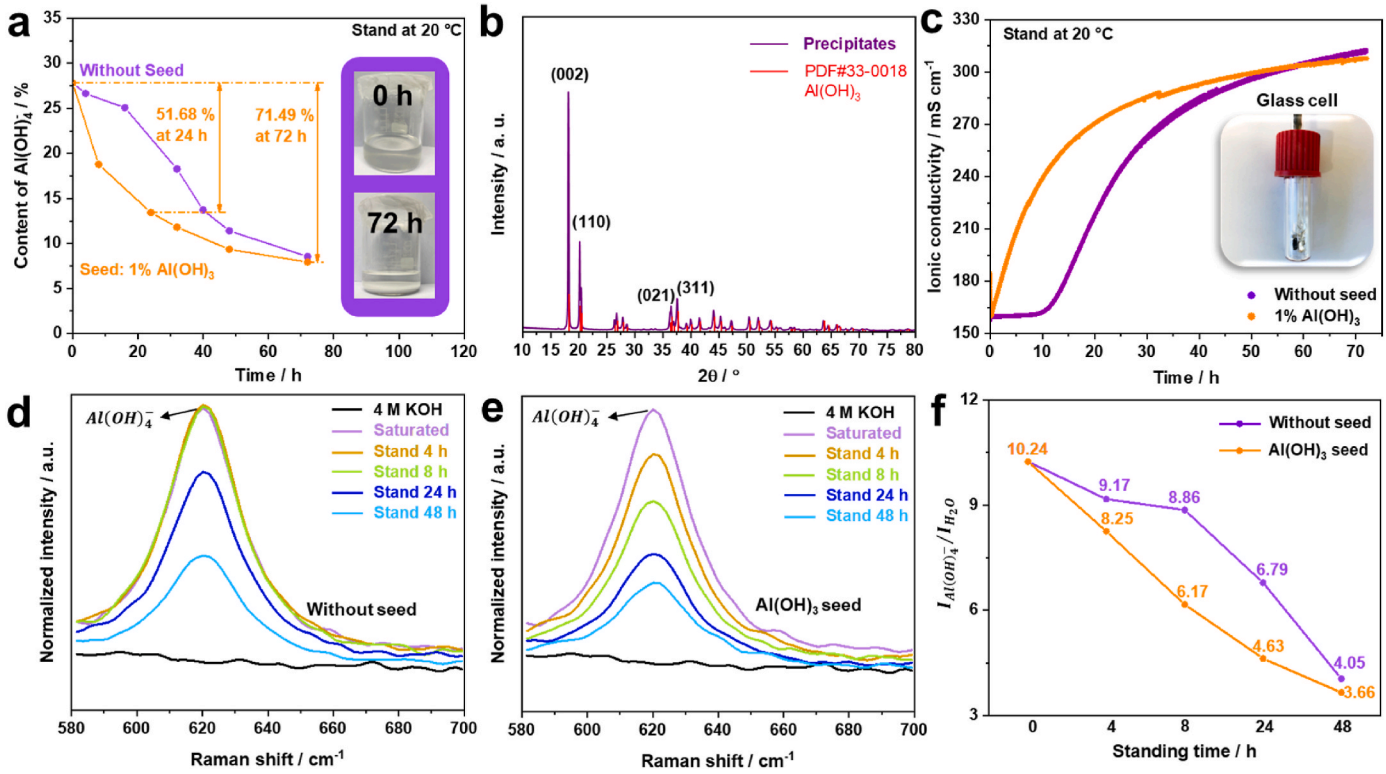

Fig. 3. Characterization of the precipitation process via standing the sample at 20 °C. The samples were prepared at 50 °C by adding 4 g Al powder into 60 mL 4 M KOH solution. (a) Al content tested via ICP-OES measurements of the upper solution after various standing time. The sample with/without the addition of $Al(OH)_3$ as the seed are plotted in orange and purple, respectively. Insets show the photography of the sample without $Al(OH)_3$ seed at the initial state and after standing at 20 °C for 72 h. (b) XRD spectrum of the white precipitate collected from the saturated solution without seeds after standing 72 h at 20 °C. (c) Ionic conductivity of the saturated solution along the precipitation process at 20 °C. The inset shows the glass conductivity cell equipped with two platinized-platinum electrodes. Raman spectra of the upper solution extracted from the samples (d) without and (e) with 1% $Al(OH)_3$ seed after different standing times at 20 °C, and corresponding (f) $Al(OH)_4^-$ (620 cm^{-1})/H_2O (1640 cm^{-1}) peak intensity ratio. (For interpretation of the references to colour in this figure legend, the reader is referred to the Web version of this article.)

20 °C for 40 and 72 h, about 50% and 70% of $Al(OH)_4^-$ initially present in the solution was removed, respectively.

It is also observed that the Al concentration decreases slowly in the initial 16 h than afterward, which has been confirmed with two additional experiments for reproducibility (Fig. S12). Thus, such an initial hysteresis is probably related to the nucleation process. In fact, the process is accelerated by adding 1% commercial $Al(OH)_3$ powder seeds (XRD pattern is shown in Fig. S13). As shown in Fig. 3a, the content of $Al(OH)_4^-$ in the solution dropped to 48.32% of the initial one after only 24 h. After the solution without seeds stood at 20 °C for 72 h, the white precipitation was collected, washed, and dried at 60 °C under vacuum overnight. XRD pattern (Fig. 3b) reveals that the white precipitate is $Al(OH)_3$.

To further study the precipitation process, the ionic conductivity evolution upon the precipitation process was monitored with glass conductivity cells equipped with platinized-platinum electrodes. The results and the photo of the cell are shown in Fig. 3c. In general, the ionic conductivity of the samples significantly increased after standing at 20 °C, which indicates the release of OH^- during the precipitation of $Al(OH)_3$. Despite the similar initial and final ionic conductivities, the ionic conductivity evolution for the samples with/without the $Al(OH)_3$ seed is different. Without the $Al(OH)_3$ seed, the ionic conductivity rise slowly in the initial 12 h because of the slow nucleation, which is identical to the ICP-OES results (Fig. 3a). Possibly affected by the different vessels and/or the presence of the platinum electrodes, the nucleation duration is shorter in the conductivity cell than in the beaker. After nucleation, the conductivity rapidly increases and finally reaches 308 mS cm^{-1} at 72 h. In contrast, the experiment with the $Al(OH)_3$ seed does not show any initial conductivity plateau, but its immediate increase from 160 to 279 mS cm^{-1} after only 24 h.

To confirm the variation of $Al(OH)_4^-$ in the electrolyte upon the precipitation process, Raman spectra of the samples after various standing times were measured. The full spectra in the range of 400–1800 cm^{-1} are shown in Fig. S14. The peak at 620 cm^{-1} originates from $Al(OH)_4^-$ [58], while the broad peak at 1640 cm^{-1} is assigned to H_2O [59]. The $Al(OH)_4^-$ peaks with the intensity normalized to that of the H_2O peak are shown in Fig. 3d and e. In general, the intensity of the $Al(OH)_4^-$ peak decreases with standing time. The relative peak intensity (R) of $Al(OH)_4^-$ with respect to that of H_2O (Fig. 3f and Table S5) shows a downward trend with standing time, proving a decreasing $Al(OH)_4^-$ concentration upon the precipitation process. Compared with the seed-free solution, the seeded one exhibits faster decrease of the $Al(OH)_4^-$ peak intensity in the first 8 h, which can be explained by the seed-promoted nucleation.

These results collaboratively prove that dissolved $Al(OH)_4^-$ can be effectively converted to insoluble $Al(OH)_3$ with the release of OH^- via the seed-aided precipitation process in relatively short times, in principle allowing for the regeneration of the electrolyte and the recovery of the voltage decay in Al-air full cells. Moreover, the converted $Al(OH)_3$, after being calcined to Al_2O_3, can be used for smelting Al. This enables a fully-circular energy storage approach, combining Al-air batteries (metal to power) and Al production (power to metal), for potential seasonable and even annual energy storage due to the easy and safe storage of Al metal.

On the other hand, it has to be considered that the use of the proposed method requires the operation of the Al-air cells at elevated temperature, i.e., 50 °C. Therefore, the electrochemical properties of AMAs at 50 °C have been evaluated also at such a temperature. First, the 4 M KOH solution saturated with 66.7 g L^{-1} of Al (S-50 electrolyte) was prepared. This was left at 20 °C for 24 and 48 h, yielding the S-50-s24 and S-50-s48 electrolytes, respectively. To suppress the self-corrosion of AMAs, 5 g L^{-1} of $Na_2SnO_3{\cdot}3H_2O$ was added to the above electrolytes before electrochemical tests.

The potential evolution of AMAs subjected to a current density of 100 mA cm^{-2} for 2 h in various electrolytes at 50 °C is shown in Fig. 4a. The CE and average potential of AMAs are summarized in Fig. S15. The Blank electrolyte leads to a low electrode potential of −1.57 V vs. Ag/AgCl and a high CE of 97.9%. Comparing these results with those obtained at 20 °C (Fig. 1b and Fig. S2), one can find that higher operation temperature leads to slightly lower CE, but much lower electrode potential, which is beneficial for higher energy density of the Al-air cells. The negative effect of the $Al(OH)_4^-$ on AMAs is also observed at the elevated temperature. When the S-50 electrolyte is employed, the CE and average potential are 95.08% and −1.23 V vs. Ag/AgCl, respectively. However, these parameters are superior to those obtained with the S-20 electrolyte at 20 °C (Fig. 1b,**S2**). Therefore, increasing the

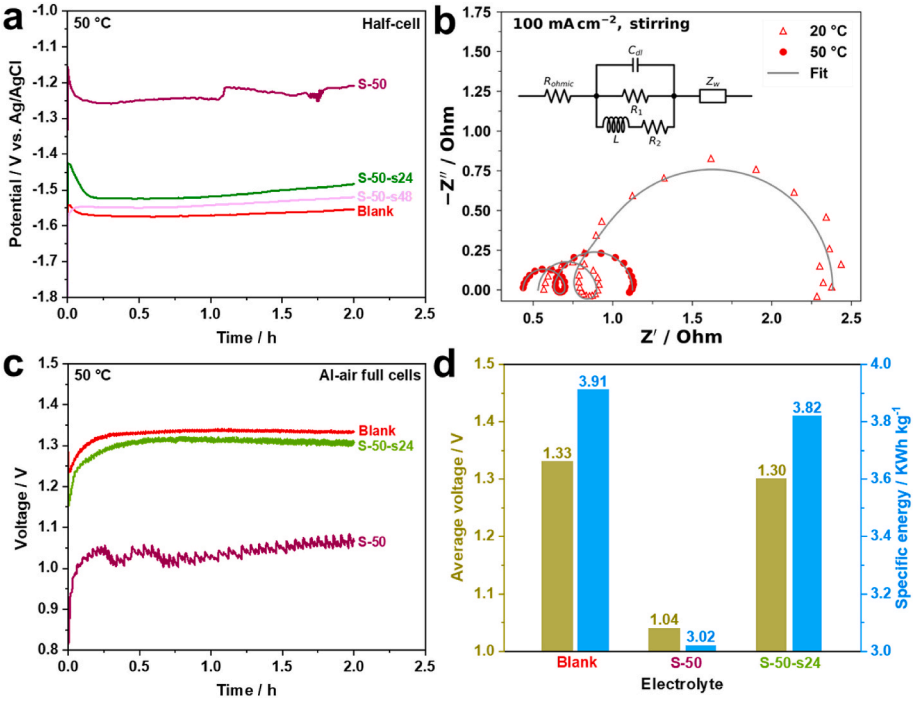

Fig. 4. (a) Potential of AMAs upon electrochemical oxidation at 100 mA cm^{-2} at 50 °C in three-electrode half cells with the Blank, S-50, S-50-s24, and S-50-s48 electrolytes. (b) Electrochemical impedance spectra of AMAs in the stirred blank electrolyte at 20 and 50 °C. (c) Galvanostatic discharge curves of Al-air full cells employing Blank, S-50, and S-50-s24 electrolytes at 100 mA cm^{-2} at 50 °C, and (d) the corresponding average voltage and specific energy (based on the mass of consumed Al).

operation temperature from 20 °C to 50 °C weakens the negative influence of the reduced OH concentration on the electrochemical reaction by increasing the ion mobility. When the regenerated electrolytes (S-50-s24 and S-50-s48) are used, all the cell parameters effectively recovered. For instance, when S-50-s24 is used, the CE and average potential are 96.7% and 1.51 V vs. Ag/AgCl. The reduced overpotential at 50 °C can be attributed to the promoted ionic transport and kinetics, as the higher operation temperature effectively reduces both the ohmic resistance and the polarization resistance of AMAs in the 4 M KOH solution as shown in the fitted EIS in Fig. 4b. The equivalent circuit model using a finite-length Warburg element to describe the LF semicircle shows a good validity, as the extracted length and diffusion coefficient are in agreement with the data at 20 °C (Table S2).

Al-air full cells with Blank, S-50, and S-50-s24 electrolytes were evaluated upon discharge current density of 100 mA cm ^{2} at 50 °C. The discharge profiles are displayed in Fig. 4c, and the corresponding CE, average discharge voltage, and specific energy based on the mass of consumed Al are shown in Fig. S16 and Fig. 4d, respectively. Compared with the Blank electrolyte, S-50 leads to slightly lower CE (98.7% vs. 97.3%) and significantly reduced discharge voltage (1.33 V vs. 1.04 V). As a consequence, the specific energy is decreased from 3.91 to 3.02 kWh kg ^{1}. When the recycled electrolyte (S-50-s24) is used, elevated CE (98.7%) and discharge voltage (1.30 V) are achieved leading to high specific energy of 3.82 kWh kg ^{1}, i.e., very close to the one obtained with the Blank electrolyte. These results demonstrate that the seed precipitation of $Al(OH)_3$ in used electrolytes enables recovering the decayed voltage and specific energy upon discharge of Al-air full cells. Moreover, the specific energy obtained with S-50-s24 at 50 °C is 2.3 times that obtained with the blank (Blank) electrolyte tested at 20 °C (Fig. S4). Therefore, increasing the operation temperature from 20 °C to 50 °C not only allows voltage recovery, but also significantly improves the electrochemical performance of Al-air full cells.

Inspired by the aforementioned results obtained via the electrolytes prepared via chemical reaction, the behavior of Al-air cells was further explored making use of the electrolyte regeneration via the proposed seeded precipitation process. Prototype Al-air cells were realized employing Al foil (1 mm thick) as the anode and MnO_x-based air cathode. About 10 mL of 4 M KOH solutions containing 5 g L ^{1} $Na_2SnO_3{\cdot}3H_2O$ as the flow electrolytes (Blank) were stored in a small tank acting as electrolyte reservoir. A peristaltic pump was used to flow the electrolyte from the reservoir into the cell in a closed circle. The cells were discharged at 100 mA cm ^{2} and 50 °C. The Al foil was nearly consumed over every 8 h at 100 mA cm ^{2} and was therefore replaced with a new Al foil. This was repeated twice without replacing neither the electrolyte nor the cathode. The cell voltage upon discharge is displayed in Fig. 5a. Due to the accumulation of $Al(OH)_4$ and consumption of OH , cell voltage decline upon discharge is observed. Note that the voltage decay is more pronounced at 20 °C due to the more negative effect of $Al(OH)_4$ accumulated in the electrolyte (Fig. S17). After discharging for 24 h (equaling 2.4 Ah), the electrolyte was extracted from the cell for regeneration. Specifically, 1% $Al(OH)_3$ seed was added to the electrolyte, which was placed in a climatic chamber at 20 °C for 24 h. Afterward, the mixture was filtered, and the clear solution was refilled to the Al-air cell as the regenerated electrolyte. The electrolyte regeneration was conducted again after discharging for additional 8 h.

The content of aluminum species in the electrolyte before and after the seeded precipitation was measured to be 25.22% and 10.36% (Fig. S18), respectively, which is basically consistent with the results in Fig. 2a and proves that the $Al(OH)_4$ generated from the electrochemical reaction of Al can also be effectively converted via the proposed seeded

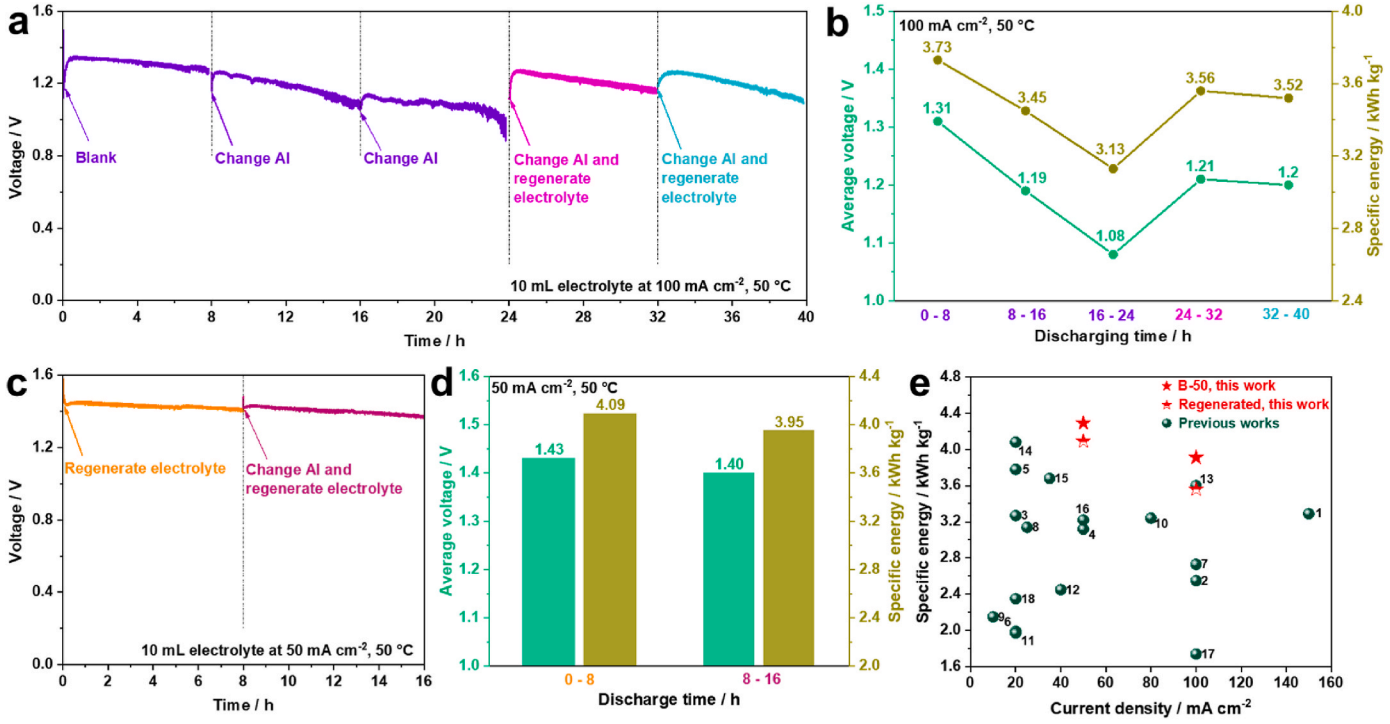

Fig. 5. (a) Voltage evolution of Al-air cells employing 10 mL electrolytes upon long-term discharge at 100 mA cm^{-2} and 50 °C. The Al foil electrode was nearly consumed after 8 h and therefore changed with a new Al foil. The same cathode was used for the whole measurement. The initial electrolyte, 4 M KOH aqueous solution with 5 g L^{-1} $Na_2SnO_3{\cdot}3H_2O$, was used for the initial 24 h. After, the electrolyte was extracted and regenerated via seeded precipitation at 20 °C. Afterward, the supernatant was refilled to the cell as the regenerated electrolyte for the following measurements. Such the electrolyte regeneration was conducted again after additional 8 h discharge. (b) Average voltage and specific energy of the Al-air cell in different periods of discharge shown in (a). (c) Voltage evolution of Al-air cells employing 10 mL regenerated electrolytes at 50 °C and 50 mA cm^{-2}. After discharge for 8 h, the AMA and electrolyte were replaced and regenerated, respectively. (d) Average voltage and specific energy of the Al-air cell in different periods of discharge shown in (c). (e) Comparison of the performance of Al-air batteries developed in this work and in the previous literature.

precipitation process. With the regenerated electrolyte, the voltage of the Al-air cell greatly recovered from 0.9 V to 1.3 V (Figs. 5a and 24–40 h). The average voltage and specific energy in the different periods of the discharge (Fig. 5a) are summarized in Fig. 5b. From 0 to 24 h, the average voltage and specific energy decreases from 1.31 V to 3.73 kWh kg ^{1} to 1.08 V and 3.13 kWh kg ^{1}, respectively, due to the formation of $Al(OH)_4$ and the consumption of OH . After the electrolyte is regenerated, however, the average cell voltage and specific energy recover to more than 1.20 V and 3.52 kWh kg ^{1} at 100 mA cm ^{2}, respectively. Additionally, the influence of current density on the electrochemical performance of Al-air cells employing the blank electrolyte was also explored (Fig. S19). At the optimized current density of 50 mA cm ^{2}, the specific energy based on the mass of the consumed Al metal reaches 4.29 kWh kg ^{1}. The electrochemical performance of Al-air cells employing the regenerated electrolyte was also evaluated at 50 mA cm ^{2}, and the voltage evolution is displayed in Fig. 5c. Under this condition, an average voltage of 1.43 V and specific energy of 4.09 kWh kg ^{1} are recorded as summarized in Fig. 5d. The specific energy delivered in this work employing the blank and regenerated electrolytes is superior to the results reported in the previous literature as summarized in Fig. 5e. The specific information about the cited reference can be found in Table S6.

Therefore, the proposed seeded precipitation of the discharge product in the electrolyte effectively enables recovering the decayed voltage and promoting the average specific energy of the cell. The materials used in the proposed Al-air full battery and seeded precipitation process are commercially available at low cost, which is good for the economic feasibility. Moreover, the easily removal of the discharge product, Al $(OH)_3$, adds values to the system because, it is used for the Al production in line with the full circularity approach, and it enables the reuse of the electrolyte further reducing the cost. Although labor is required here for the electrolyte regeneration, this can industrially optimized via the further improvement of cell design (a possible approach is depicted in Fig. S20).

4. Conclusions

The results herein presented demonstrate that the formation of $Al(OH)_4$ upon cell discharge, which reduces the OH concentration negatively affecting the transport dynamics and reaction kinetics, is responsible for the increased overpotential of AMAs and consequent voltage decay of Al-air batteries rather than the formation of the Al $(OH)_3$ layer on the electrode surface. However, $Al(OH)_4$ can be easily removed from the electrolyte via its conversion to insoluble $Al(OH)_3$ precipitate playing on its lower solubility at 20 °C than 50 °C. The released OH effectively enable recovering the decayed cell voltage and specific energy of Al-air cells. Moreover, operating the cells at 50 °C leads to further enhanced specific energy and tolerance to $Al(OH)_4$ with respect to 20 °C, due to the promoted ionic transport and kinetics. Finally, the addition of $Al(OH)_3$ seeds accelerates the precipitation process strongly shortening the nucleation process. Based on these results, prototype high-energy Al-air cells operating at 50 °C, including the removal of the discharge product to regenerate the electrolyte, have been realized demonstrating that the decay of the voltage and specific energy upon discharge could be effectively recovered via the seeded precipitation of $Al(OH)_3$ at 20 °C.

Overall, the proposed Al-air system after further optimization and scale-up, could be combined with Al smelting (employing $Al(OH)_3$ as starting material) for the fully circular, long-term (seasonal/annual) energy storage.

CRediT authorship contribution statement

Cheng Xu: Methodology, Investigation, Writing – original draft. **Niklas Herrmann:** Formal analysis, Writing – review & editing. **Xu Liu:** Conceptualization, Writing – review & editing, Project administration. **Birger Horstmann:** Formal analysis, Writing – review & editing. **Stefano Passerini:** Writing – review & editing, Supervision, Funding acquisition.

Declaration of competing interest

The authors declare that they have no known competing financial interests or personal relationships that could have appeared to influence the work reported in this paper.

Data availability

Data will be made available on request.

Acknowledgments

C.X. and X.L. gratefully acknowledges the financial support from the Chinese Scholarship Council (CSC). The research leading to these results has received funding from Karlsruhe Institute of Technology for the project ALU-STORE (Aluminium Metal as Energy Carrier for Seasonal Energy Storage) and from the Federal Ministry of Education and Research (BMBF) in the framework of the project 'ZIB' (FKZ 03XP0204A). Jason Lelovas is acknowledged for conducting ICP-OES measurements. Dr. Jing-Dong Guo of ENERGIZER is acknolowledged for providing the air cathode.

References

[1] S. Fankhauser, S.M. Smith, M. Allen, K. Axelsson, T. Hale, C. Hepburn, J. M. Kendall, R. Khosla, J. Lezaun, E. Mitchell-Larson, M. Obersteiner, L. Rajamani, R. Rickaby, N. Seddon, T. Wetzer, The meaning of net zero and how to get it right, Nat. Clim. Change 12 (2022) 15–21, https://doi.org/10.1038/s41558-021-01245-w.

[2] J. Rogelj, M. den Elzen, N. Höhne, T. Fransen, H. Fekete, H. Winkler, R. Schaeffer, F. Sha, K. Riahi, M. Meinshausen, Paris Agreement climate proposals need a boost to keep warming well below 2 °C, Nature 534 (2016) 631–639, https://doi.org/10.1038/nature18307.

[3] M.S. Ziegler, J.M. Mueller, G.D. Pereira, J. Song, M. Ferrara, Y.-M. Chiang, J. E. Trancik, Storage requirements and costs of shaping renewable energy toward grid decarbonization, Joule 3 (2019) 2134–2153, https://doi.org/10.1016/j.joule.2019.06.012.

[4] C.M. Grams, R. Beerli, S. Pfenninger, I. Staffell, H. Wernli, Balancing Europe's wind-power output through spatial deployment informed by weather regimes, Nat. Clim. Change 7 (2017) 557–562, https://doi.org/10.1038/nclimate3338.

[5] J.A. Rabinowitz, M.W. Kanan, The future of low-temperature carbon dioxide electrolysis depends on solving one basic problem, Nat. Commun. 11 (2020) 5231, https://doi.org/10.1038/s41467-020-19135-8.

[6] H. Ersoy, M. Baumann, L. Barelli, A. Ottaviano, L. Trombetti, M. Weil, S. Passerini, Hybrid energy storage and hydrogen supply based on aluminum—a multiservice case for electric mobility and energy storage services, Adv. Mater. Technol. 7 (2022), 2101400, https://doi.org/10.1002/admt.202101400.

[7] A. Sternberg, A. Bardow, Power-to-What?-Environmental assessment of energy storage systems, Energy Environ. Sci. 8 (2015) 389–400, https://doi.org/10.1039/c4ee03051f.

[8] T.M. Gür, Review of electrical energy storage technologies, materials and systems: challenges and prospects for large-scale grid storage, Energy Environ. Sci. 11 (2018) 2696–2767, https://doi.org/10.1039/c8ee01419a.

[9] M.Y. Haller, D. Amstad, M. Dudita, A. Englert, A. Häberle, Combined heat and power production based on renewable aluminium-water reaction, Renew. Energy 174 (2021) 879–893, https://doi.org/10.1016/j.renene.2021.04.104.

[10] J. Ryu, M. Park, J. Cho, Advanced technologies for high-energy aluminum–air batteries, Adv. Mater. 31 (2019) 1–8, https://doi.org/10.1002/adma.201804784.

[11] R. Mori, Recent developments for aluminum–air batteries, Electrochem. Energy Rev. 3 (2020) 344–369, https://doi.org/10.1007/s41918-020-00065-4.

[12] R. Buckingham, T. Asset, P. Atanassov, Aluminum-air batteries: a review of alloys, electrolytes and design, J. Power Sources 498 (2021), 229762, https://doi.org/10.1016/j.jpowsour.2021.229762.

[13] M. Baumann, L. Barelli, S. Passerini, The potential role of reactive metals for a clean energy transition, Adv. Energy Mater. 10 (2020), 2001002, https://doi.org/10.1002/aenm.202001002.

[14] Y. Liu, Q. Sun, W. Li, K.R. Adair, J. Li, X. Sun, A comprehensive review on recent progress in aluminum–air batteries, Green Energy Environ 2 (2017) 246–277, https://doi.org/10.1016/j.gee.2017.06.006.

[15] L. Fan, H. Lu, J. Leng, Performance of fine structured aluminum anodes in neutral and alkaline electrolytes for Al-air batteries, Electrochim. Acta 165 (2015) 22–28, https://doi.org/10.1016/j.electacta.2015.03.002.

[16] M. Jiang, C. Fu, R. Cheng, W. Zhang, T. Liu, R. Wang, J. Zhang, B. Sun, Integrated and binder-free air cathodes of Co3Fe7 nanoalloy and Co5.47N encapsulated in nitrogen-doped carbon foam with superior oxygen reduction activity in flexible aluminum-air batteries, Adv. Sci. 7 (2020), 200747, https://doi.org/10.1002/advs.202000747.

[17] J. Ma, J. Wen, J. Gao, Q. Li, Performance of Al–0.5 Mg–0.02 Ga–0.1 Sn–0.5 Mn as anode for Al–air battery in NaCl solutions, J. Power Sources 253 (2014) 419–423, https://doi.org/10.1016/j.jpowsour.2013.12.053.

[18] G.A. Elia, K. Marquardt, K. Hoeppner, S. Fantini, R. Lin, E. Knipping, W. Peters, J. F. Drillet, S. Passerini, R. Hahn, An overview and future perspectives of aluminum batteries, Adv. Mater. 28 (2016) 7564–7579, https://doi.org/10.1002/adma.201601357.

[19] M. Jiang, C. Fu, P. Meng, J. Ren, J. Wang, J. Bu, A. Dong, J. Zhang, W. Xiao, B. Sun, Challenges and strategies of low-cost aluminum anodes for high-performance Al-based batteries, Adv. Mater. 34 (2022), 2102026, https://doi.org/10.1002/adma.202102026.

[20] S. Wu, S. Hu, Q. Zhang, D. Sun, P. Wu, Y. Tang, H. Wang, Hybrid high-concentration electrolyte significantly strengthens the practicability of alkaline aluminum-air battery, Energy Storage Mater. 31 (2020) 310–317, https://doi.org/10.1016/j.ensm.2020.06.024.

[21] L. Fan, H. Lu, The effect of grain size on aluminum anodes for Al–air batteries in alkaline electrolytes, J. Power Sources 284 (2015) 409–415, https://doi.org/10.1016/j.jpowsour.2015.03.063.

[22] Y.-J. Cho, I.-J. Park, H.-J. Lee, J.-G. Kim, Aluminum anode for aluminum–air battery – Part I: influence of aluminum purity, J. Power Sources 277 (2015) 370–378, https://doi.org/10.1016/j.jpowsour.2014.12.026.

[23] S.Z. El Abedin, F. Endres, Electrochemical behaviour of Al, Al—in and Al–Ga–in alloys in chloride solutions containing zinc ions, J. Appl. Electrochem. 34 (2004) 1071–1080, https://doi.org/10.1023/B:JACH.0000042672.23588.df.

[24] S. Liu, J. Ban, H. Shi, Z. Wu, G. Shao, Near solution-level conductivity of polyvinyl alcohol based electrolyte and the application for fully compliant Al-air battery, Chem. Eng. J. 431 (2022), 134283, https://doi.org/10.1016/j.cej.2021.134283.

[25] Q. Zhao, P. Wu, D. Sun, H. Wang, Y. Tang, A dual-electrolyte system for highly efficient Al-air batteries, Chem. Commun. 58 (2022) 3282–3285, https://doi.org/10.1039/d1cc07044d.

[26] C. Zhu, H. Yang, A. Wu, D. Zhang, L. Gao, T. Lin, Modified alkaline electrolyte with 8-hydroxyquinoline and ZnO complex additives to improve Al-air battery, J. Power Sources 432 (2019) 55–64, https://doi.org/10.1016/j.jpowsour.2019.05.077.

[27] Q.X. Kang, T.Y. Zhang, X. Wang, Y. Wang, X.Y. Zhang, Effect of cerium acetate and L-glutamic acid as hybrid electrolyte additives on the performance of Al–air battery, J. Power Sources 443 (2019), 227251, https://doi.org/10.1016/j.jpowsour.2019.227251.

[28] H.A. El Shayeb, F.M. Abd El Wahab, S. Zein El Abedin, Electrochemical behaviour of Al, Al–Sn, Al–Zn and Al–Zn–Sn alloys in chloride solutions containing stannous ions, Corrosion Sci. 43 (2001) 655–669, https://doi.org/10.1016/S0010-938X(00)00101-3.

[29] C.D.S. Tuck, J.A. Hunter, G.M. Scamans, The electrochemical behavior of Al-Ga alloys in alkaline and neutral electrolytes, J. Electrochem. Soc. 134 (1987) 2970, https://doi.org/10.1149/1.2100325.

[30] S. Palanisamy, N. Rajendhran, S. Srinivasan, A.P. Shyma, V. Murugan, B. Parasuraman, S. Kheawhom, A novel nano-YSZ-Al alloy anode for Al–air battery, J. Appl. Electrochem. 51 (2021) 345–356, https://doi.org/10.1007/s10800-020-01493-2.

[31] C. Zhang, Z. Cai, R. Wang, P. Yu, H. Liu, Z. Wang, Enhancing the electrochemical performance of Al-Mg-Sn-Ga alloy anode for Al-air battery by solution treatment, J. Electrochem. Soc. 168 (2021), 030519, https://doi.org/10.1149/1945-7111/abe9c6.

[32] J. Liu, D. Wang, D. Zhang, L. Gao, T. Lin, Synergistic effects of carboxymethyl cellulose and ZnO as alkaline electrolyte additives for aluminium anodes with a view towards Al-air batteries, J. Power Sources 335 (2016) 1–11, https://doi.org/10.1016/j.jpowsour.2016.09.060.

[33] C. Lv, Q. Zhang, Y. Zhang, Z. Yang, P. Wu, D. Huang, H. Li, H. Wang, Y. Tang, Synergistic regulating the aluminum corrosion by ellagic acid and sodium stannate hybrid additives for advanced aluminum-air battery, Electrochim. Acta 417 (2022), 140311, https://doi.org/10.1016/j.electacta.2022.140311.

[34] P. Sun, J. Chen, Y. Huang, J.-H. Tian, S. Li, G. Wang, Q. Zhang, Z. Tian, L. Zhang, High-Strength agarose gel electrolyte enables long-endurance wearable Al-air batteries with greatly suppressed self-corrosion, Energy Storage Mater. 34 (2021) 427–435, https://doi.org/10.1016/j.ensm.2020.10.009.

[35] S. Wu, Q. Zhang, D. Sun, J. Luan, H. Shi, S. Hu, Y. Tang, H. Wang, Understanding the synergistic effect of alkyl polyglucoside and potassium stannate as advanced hybrid corrosion inhibitor for alkaline aluminum-air battery, Chem. Eng. J. 383 (2020), 123162, https://doi.org/10.1016/j.cej.2019.123162.

[36] Y. Xue, H. Huang, H. Miao, S. Sun, Q. Wang, S. Li, Z. Liu, One-pot synthesis of La0.7Sr0.3MnO3 supported on flower-like CeO2 as electrocatalyst for oxygen reduction reaction in aluminum-air batteries, J. Power Sources 358 (2017) 50–60, https://doi.org/10.1016/j.jpowsour.2017.05.027.

[37] S. Sun, Y. Xue, Q. Wang, H. Huang, H. Miao, Z. Liu, Cerium ion intercalated MnO2 nanospheres with high catalytic activity toward oxygen reduction reaction for aluminum-air batteries, Electrochim. Acta 263 (2018) 544–554, https://doi.org/10.1016/j.electacta.2018.01.057.

[38] E.S. Davydova, I.N. Atamanyuk, A.S. Ilyukhin, E.I. Shkolnikov, A.Z. Zhuk, Nitrogen-doped carbonaceous catalysts for gas-diffusion cathodes for alkaline aluminum-air batteries, J. Power Sources 306 (2016) 329–336, https://doi.org/10.1016/j.jpowsour.2015.11.112.

[39] J. Li, N. Zhou, J. Song, L. Fu, J. Yan, Y. Tang, H. Wang, Cu–MOF-Derived Cu/Cu2O nanoparticles and CuNxCy species to boost oxygen reduction activity of ketjenblack carbon in Al–air battery, ACS Sustain. Chem. Eng. 6 (2018) 413–421, https://doi.org/10.1021/acssuschemeng.7b02661.

[40] J. Liu, C. Zhang, S. Yuan, W. Yang, Y. Cao, J. Deng, B. Xu, H. Lu, CoP-decorated N, P-doped necklace-like carbon for highly efficient oxygen reduction and Al-air batteries, Chem. Eng. J. 428 (2022), 131326, https://doi.org/10.1016/j.cej.2021.131326.

[41] Y. Li, Y. Wang, S. Zhang, L. Miao, M. Wei, K. Wang, Corrosion inhibition of aromatic acids on Al-7075 anode for Al-air batteries with alkaline electrolyte, J. Power Sources 523 (2022), 231042, https://doi.org/10.1016/j.jpowsour.2022.231042.

[42] P. Zhang, J. Xue, X. Liu, Z. Wang, X. Li, K. Jiang, Electrochimica Acta Improving energy efficiency of commercial aluminum alloy as anodes for Al-air battery through introducing micro-nanoscale AlSb precipitates, Electrochim. Acta 417 (2022), 140331, https://doi.org/10.1016/j.electacta.2022.140331.

[43] P. Wu, Q. Zhao, H. Yu, Z. Tang, Y. Li, D. Huang, D. Sun, H. Wang, Y. Tang, Modification on water electrochemical environment for durable Al-Air Battery: achieved by a Low-Cost sucrose additive, Chem. Eng. J. 438 (2022), 135538, https://doi.org/10.1016/j.cej.2022.135538.

[44] Z. Wang, H. Zhou, J. Xue, X. Liu, S. Liu, X. Li, D. He, Ultrasonic-assisted hydrothermal synthesis of cobalt oxide/nitrogen-doped graphene oxide hybrid as oxygen reduction reaction catalyst for Al-air battery, Ultrason. Sonochem. 72 (2021), 105457, https://doi.org/10.1016/j.ultsonch.2020.105457.

[45] S. Liu, Z. Cao, Y. Meng, Y. Li, W. Yang, Z. Chang, W. Liu, X. Sun, Aerophilic Co-embedded N-doped carbon nanotube arrays as highly efficient cathodes for aluminum-air batteries, ACS Appl. Mater. Interfaces 13 (2021) 26853–26860, https://doi.org/10.1021/acsami.1c00837.

[46] S. Wu, Q. Zhang, J. Ma, D. Sun, Y. Tang, H. Wang, Interfacial design of Al electrode for efficient aluminum-air batteries: issues and advances, Mater. Today Energy 18 (2020), 100499, https://doi.org/10.1016/j.mtener.2020.100499.

[47] A.V. Ilyukhina, B.V. Kleymenov, A.Z. Zhuk, Development and study of aluminum-air electrochemical generator and its main components, J. Power Sources 342 (2017) 741–749, https://doi.org/10.1016/j.jpowsour.2016.12.105.

[48] A.A. Mohamad, Electrochemical properties of aluminum anodes in gel electrolyte-based aluminum-air batteries, Corrosion Sci. 50 (2008) 3475–3479, https://doi.org/10.1016/j.corsci.2008.09.001.

[49] C. Lv, Y. Zhang, J. Ma, Y. Zhu, D. Huang, Y. Li, H. Wang, Y. Tang, Regulating solvation and interface chemistry to inhibit corrosion of the aluminum anode in aluminum-air batteries, J. Mater. Chem. A. 10 (2022) 9506–9514, https://doi.org/10.1039/d2ta01064j.

[50] X.X. Zeng, J.M. Wang, Q.L. Wang, D.S. Kong, H.B. Shao, J.Q. Zhang, C.N. Cao, The effects of surface treatment and stannate as an electrolyte additive on the corrosion and electrochemical performances of pure aluminum in an alkaline methanol–water solution, Mater. Chem. Phys. 121 (2010) 459–464, https://doi.org/10.1016/j.matchemphys.2010.02.006.

[51] K.-K. Lee, K.-B. Kim, Electrochemical impedance characteristics of pure Al and Al–Sn alloys in NaOH solution, Corrosion Sci. 43 (2001) 561–575, https://doi.org/10.1016/S0010-938X(00)00060-3.

[52] H.B. Shao, J.M. Wang, Z. Zhang, J.Q. Zhang, C.N. Cao, Electrochemical impedance spectroscopy analysis on the electrochemical dissolution of aluminum in an alkaline solution, J. Electroanal. Chem. 549 (2003) 145–150, https://doi.org/10.1016/S0022-0728(03)00266-3.

[53] F. Single, B. Horstmann, A. Latz, Theory of impedance spectroscopy for lithium batteries, J. Phys. Chem. C 123 (2019) 27327–27343, https://doi.org/10.1021/acs.jpcc.9b07389.

[54] A.J. Vadim F. LvovichWiley, Electrochemical Impedance Spectroscopy (EIS): A Review Study of Basic Aspects of the Corrosion Mechanism Applied to Steels, 2012.

[55] H.B. Shao, J.M. Wang, Z. Zhang, J.Q. Zhang, C.N. Cao, Electrochemical impedance spectroscopy analysis on the electrochemical dissolution of aluminum in an alkaline solution, J. Electroanal. Chem. 549 (2003) 145–150, https://doi.org/10.1016/S0022-0728(03)00266-3.

[56] S. Clark, A. Latz, B. Horstmann, Rational development of neutral aqueous electrolytes for zinc–air batteries, ChemSusChem 10 (2017) 4735–4747, https://doi.org/10.1002/cssc.201701468.

[57] S. Clark, A.R. Mainar, E. Iruin, L.C. Colmenares, J.A. Blázquez, J.R. Tolchard, Z. Jusys, B. Horstmann, Designing aqueous organic electrolytes for zinc–air batteries: method, simulation, and validation, Adv. Energy Mater. 10 (2020), 1903470, https://doi.org/10.1002/aenm.201903470.

[58] B.M. Lu, X.Y. Jin, J. Tang, S.P. Bi, DFT studies of Al-O Raman vibrational frequencies for aquated aluminium species, J. Mol. Struct. 982 (2010) 9–15, https://doi.org/10.1016/j.molstruc.2010.07.012.

[59] E.D. Palik, H.F. Gray, P.B. Klein, A Raman study of etching silicon in aqueous KOH, J. Electrochem. Soc. 130 (1983) 956–959, https://doi.org/10.1149/1.2119866.